



Bi₃TeBO₉: electronic structure, optical properties and photoinduced phenomena

A. Majchrowski¹, M. Chronik¹, M. Rudysh^{2,3}, M. Piasecki^{2,*} , K. Ozga⁵, G. Lakshminarayana⁴, and I. V. Kityk⁵

¹Institute of Applied Physics, Military University of Technology, 2 Kaliskiego Str., 00-908 Warsaw, Poland

²Institute of Physics, Jan Długosz University, 13/15 Armii Krajowej Str., 42-201 Częstochowa, Poland

³Faculty of Physics, Ivan Franko National University of Lviv, 8 Kyrylo and Mefodiy Str., Lviv 79005, Ukraine

⁴Wireless and Photonic Networks Research Centre, Faculty of Engineering, Universiti Putra Malaysia, 43400 Serdang, Selangor, Malaysia

⁵Institute of Optoelectronics and Measuring Systems, Faculty of Electrical Engineering, Częstochowa University of Technology, 17 Armii Krajowej Str., 42-200 Częstochowa, Poland

Received: 1 July 2017

Accepted: 4 September 2017

Published online:

14 September 2017

© The Author(s) 2017. This article is an open access publication

ABSTRACT

Improvement of the nonlinear optical properties, mainly photoinduced enhancement of effective second harmonic generation was observed in Bi₃TeBO₉ (BTBO) crystals under irradiation of two external UV laser beams. The effect is caused by an interaction of two coherent photoinducing beams of nitrogen laser with wavelength 371 nm near the Bi₃TeBO₉ fundamental edge, resulting in formation of additional anisotropy. To explain the observed phenomenon and establish the general features of the electronic structure, the band structure calculations, as well as electronic density of states, elastic properties and principal optical functions were simulated by means of the density functional theory approach. The comparison of the nonlinear optical properties with the conventional α -BIBO crystal shows that BTBO is a promising material for the fabrication of UV laser optical triggers.

Introduction

The search for novel inorganic materials for nonlinear optics is an important direction of modern optoelectronics [1–4]. Representative applications of such materials are: second harmonic generation (SHG), optical parametric oscillation (OPO), optical parametric amplification (OPA) and self-frequency doubling (SFD). The materials should work in possibly broadest

spectral range, from near infrared (NIR) to ultraviolet (UV). Among such materials, a particular role belongs to borate crystals, i.e., β -BaB₂O₄, LiB₃O₅, KBe₂BO₃F₂, CsLiB₆O₁₀, La₂CaB₁₀O₁₉ and α -BiB₃O₆. In general, borates are mechanically and chemically stable, possess wide transparency range, have good optical quality and are characterized with high nonlinear optical coefficients [5]. For such materials, the main efforts are devoted to manipulation by the cationic

Address correspondence to E-mail: m.piasecki@ajd.czest.pl

subsystem in connection with principal anionic borate clusters like $[\text{BO}_3]$, $[\text{BO}_4]$, $[\text{B}_3\text{O}_6]$, $[\text{B}_3\text{O}_7]$, $[\text{B}_2\text{O}_7]$ or $[\text{B}_2\text{O}_5]$, etc., in order to achieve the highest second-order nonlinear optical susceptibilities, which are determined by microscopic hyperpolarizabilities.

Recently, Bi_3TeBO_9 (BTBO) crystal, having very large second-order nonlinear optical susceptibilities, was discovered [6, 7]. The preliminary data indicate that its nonlinear optical coefficients are, respectively, higher than in the case of the exceptional $\alpha\text{-BiB}_3\text{O}_6$ ($\alpha\text{-BIBO}$) compound [7].

Moreover, following the general considerations one can expect that the titled compound maybe a promising medium for the laser-operated nonlinear optical effects. For this reason, we will explore the changes of its nonlinear optical properties after illumination near the absorption edge. Additionally, the elastic properties of this material should play here crucial role. In this case, we will perform the band-structure calculations.

In the present work, we report the synthesis of BTBO powders, determine crystal structure and finally show almost 10%-relative enhancement of the existing second order nonlinear optical susceptibilities under additional two-beam coherent UV laser light treatment with wavelength near the absorption edge of BTBO.

Experimental

Powder synthesis and XRD phase analysis

BTBO powders were synthesized by means of conventional solid-state reaction route, similarly to the procedure described by Daub et al. [6]. The molar ratio of used precursor compounds: Bi_2O_3 (SIAL, 99.95%), TeO_2 (MERCK, 99.99%) and B_2O_3 (SIAL, 99.999%), was 3:2:1.1, respectively. The 5% excess of boron oxide was used to prevent the non-stoichiometry due to the presence of water and possible evaporation of B_2O_3 at elevated temperatures. The precursor compounds were mixed and thoroughly ground in an agate mortar till the homogeneous mixture was obtained. It was initially preheated at 450 °C for 12 h to evaporate the residuals of adsorbed water. In the following steps, the mixture was ground and calcined three times at 690 °C for 12 h each time. After the final grounding, the pure, white powders of BTBO were obtained. Their phase uniformity was confirmed using the XRD analysis. The

diffraction pattern of synthesized BTBO powder was collected using the BRUKER D8 Discover, equipped with standard CuK_α radiator ($\lambda_{\text{K}\alpha 1} = 1.54056 \text{ \AA}$, $\lambda_{\text{K}\alpha 2} = 1.54439 \text{ \AA}$, Siemens KFL CU 2 K, 40 kV voltage and 40 mA current in operating mode). The radiator was equipped with Göbel FGM2 mirror. The Bragg–Brentano diffraction geometry was applied. The diffraction angle $2\theta_{\text{B}}$ range was set to 10–70° with a step of 0.015° and acquisition time 2 s per step. The measurements were done at 25 °C in the temperature-stabilized Anton Paar HTK 1200N chamber. For the data processing, the DIFFRAC.SUITE EVA application was used. The $\lambda_{\text{K}\alpha 2}$ signal component was deconvoluted and removed, the background was subtracted and the data were smoothed using fast Fourier transform (FFT). The phase analysis was performed with support of Crystallography Open Database (COD). For crystallographic calculations, the MAUD ver. 2.32 program was used, allowing to perform the Rietveld refinement and calculate the precise unit cell parameters. The reference CIF file used for this analysis was received from the supplementary data given in Ref. [7]. The obtained BTBO powder diffraction pattern is shown in Fig. 1.

Methods of calculation

Calculations of the electronic, optical and elastic properties of BTBO crystal were performed within the

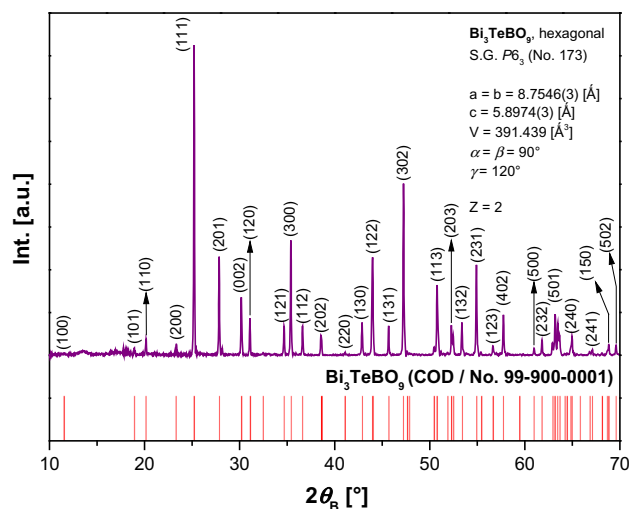


Figure 1 Experimental powder diffraction pattern (top, purple plot) for synthesized BTBO and calculated theoretical Bragg's positions (bottom, red markers) based on COD database CIF file. Presented precise unit cell parameters were determined using Rietveld refinement.

framework of density functional theory (DFT) implemented in CASTEP (Cambridge Serial Total Energy Package) program—package of Biovia Materials Studio 8.0 [8]. The initial BTBO crystal structure was taken from Ref. [7]. We applied the plane-wave (PW) basis set. Eigen function and the eigenvalues were estimated from self-consistent solving of the one-electron Kohn–Sham equation. Exchange and correlation effects were taken into account by using local-density approximation (LDA) with Ceperley–Alder–Perdew–Zunger parameterization [9, 10] and generalized gradient approximation (GGA) together with Perdew–Burke–Ernzerhof parameterization [11]. The cutoff energy of plane-wave basis was set to be equal to $E_{\text{cut}} = 830$ eV. The Monkhorst–Pack k -points grid sampling was set at $2 \times 2 \times 2$ points for the Brillouin zone used for electronic charge density calculations and geometry optimizations, respectively. Both the cell parameters and atomic positions were optimized (relaxed) using Broyden–Fletcher–Goldfarb–Shanno (BFGS) algorithm [12], until the force on each ion was smaller than 0.01 eV/Å. The resulting structures were then used as input to the electronic structures and related properties calculations.

The core electron orbitals were calculated using the norm-conserving pseudopotential (NCPP). The following electron configurations were used: B— $2s^2 2p^1$, O— $2s^2 2p^4$, Te— $5s^2 5p^4$, Bi— $5d^{10} 6s^2 6p^3$. The convergence parameters were as follows: total energy tolerance 5×10^{-6} eV/atom, maximum force tolerance 1×10^{-2} eV/Å, maximum stress component 0.02 GPa and maximum displacement 5.0×10^{-4} Å. The band structure was calculated at the following points and along directions of high symmetry of BZ: $\Gamma \rightarrow A \rightarrow H \rightarrow K \rightarrow \Gamma \rightarrow M \rightarrow L \rightarrow H$ (see Fig. 2).

Results and discussion

Structural properties

The crystal structure of BTBO crystal is presented in Fig. 3. BTBO belongs to hexagonal symmetry (space group $P6_3$, no. 173) with $Z = 2$. The experimental and theoretically calculated principal band structure parameters, using DFT-LDA and DFT-GGA exchange-correlation functionals, together with NCPP, after the optimization of lattice geometry are presented in Table 1. Following Table 1, the calculated lattice constants are in good agreement with the

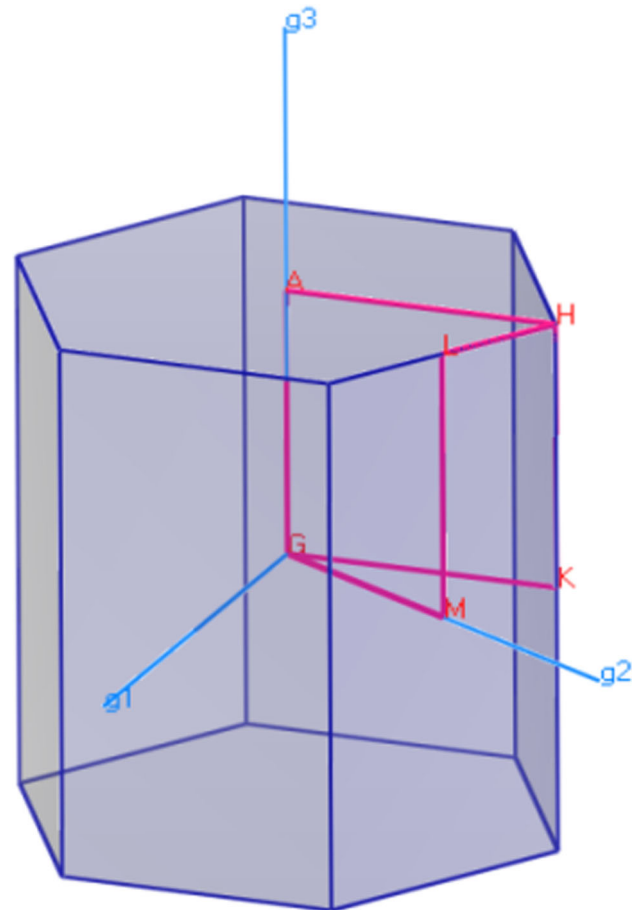


Figure 2 Brillouin zone of BTBO crystal with principal symmetry points.

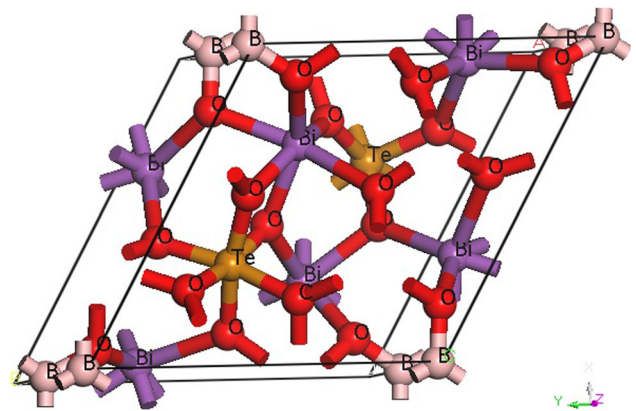


Figure 3 Visualization of BTBO unit cell crystal structure.

experimental ones. Lattice constants calculated using the LDA functional are a bit smaller than the experimental ones, while in the case of GGA functional, these parameters are a bit higher. It can be explained by the renormalization of principal electronic

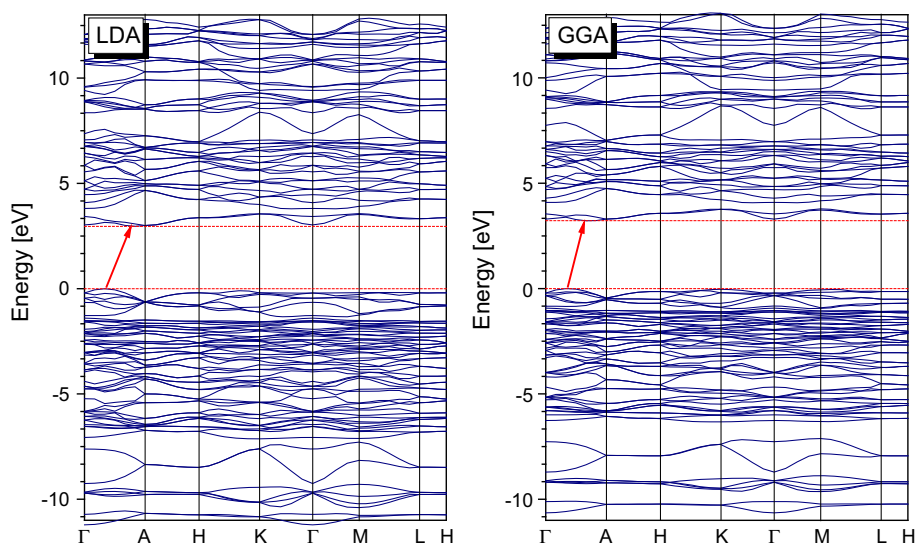
Table 1 Experimental and theoretical lattice constants calculated using Rietveld refinement, DFT–LDA and DFT–GGA exchange–correlation functionals together with NCPP

Source	a [Å]	c [Å]	a/c	V [Å ³]
This work				
LDA	8.512	5.621	1.514	352.70
GGA	8.768	5.842	1.501	388.95
Rietveld	8.7546 (3)	5.8974 (3)	1.485	391.439
Daub et al. [6]	8.751	5.898	1.484	391.16

parameters within the LDA functional, which leads to underestimation of basic structural parameters.

Electronic properties

For calculations of electronic structure and other properties, the optimized crystal structure was used. Calculated band structure of BTBO crystal using LDA and GGA functionals for exchange–correlation effects description is shown in Fig. 4. Band structure is plotted at following BZ line directions: $\Gamma \rightarrow A \rightarrow H \rightarrow K \rightarrow \Gamma \rightarrow M \rightarrow L \rightarrow H$. One can see that the band structure has a large dispersion. The lowest dispersion is observed for $A \rightarrow H$ and $L \rightarrow H$ BZ directions. Valence band maxima (VBM) and conduction band minima (CBM) are in the segment between the Γ and A points (Fig. 4) and are shifted in relation to each other. Thus, band gap of the titled crystal is of the indirect type. The smallest band gap value is equal to 2.96 eV for LDA and 3.21 eV for GGA, respectively (Table 2), while as previously

Figure 4 Band energy diagrams for BTBO crystal calculated using LDA and GGA exchange–correlation functionals.**Table 2** Band energy gap value of BTBO crystal calculated using DFT–LDA and DFT–GGA functionals, compared to referred ones

Source	E_g [eV]
Xia et al. [7]	2.70/3.23 (exp./calc.)
LDA	2.96
GGA	3.21

reported by Xia et al. [7], the experimental and calculated values were 2.70 and 3.23 eV, respectively. So, using both LDA and GGA together with NCPP, one can perfectly describe the model of BTBO crystal, since they give good agreement with the experimental values of the band gap and lattice constants. Density of states (DOS) and partial density of states (PDOS) charts give a quick qualitative picture of the crystal electronic structure. The calculated total and partial density of states for BTBO crystal are depicted in Fig. 5.

In the spectral energy range within -15 to 10 eV, one can see two distinctive groups of peaks corresponding to principal electronic states of BTBO crystal. The first group corresponds to the energy states within the range of -10.6 to 0 eV. The $6s$ and $6p$ electrons of bismuth form bands in the range from -10.6 to -7 eV and from -6.5 to 0 eV. Also, a minor peak of $6s$ electrons is observed near 0 eV. Tellurium electrons form several peaks for $5s$ electrons, which are situated nearby -10 eV and at -4 eV, while the $5p$ electrons form peak at -8 and -1 eV, respectively. In the case of boron, the $2s$ peak at -6 eV is spectrally shifted toward relatively higher energies when

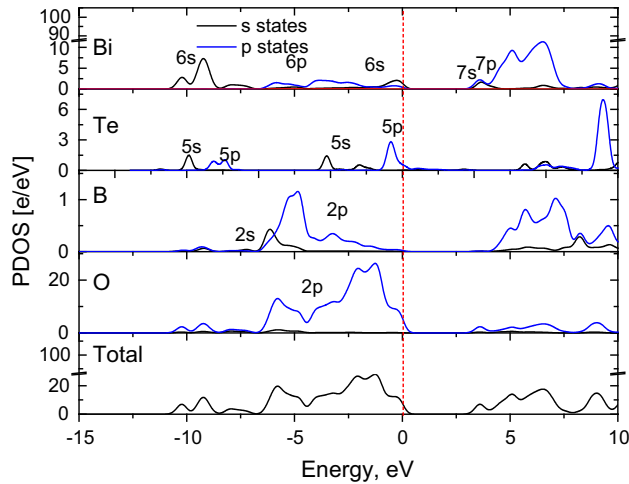


Figure 5 Total and partial density of states of BTBO crystal calculated using LDA and GGA exchange–correlation functionals.

compared to the peak formed by tellurium. Wide band originating from -6.3 to -1 eV is formed by $2p$ electrons of boron. The electrons of oxygen atoms, originating from bands that are situated in the range from -10.3 to 0 eV, correspond to $2p$ subshell. As shown in Fig. 5, the top of the valence band originates from oxygen $2p$ states, bismuth $6s$ and tellurium $5p$ states. The bottom of the conduction band is formed by p states of oxygen and s states of tellurium. It can be assumed that the optical transitions in absorption spectra are likely formed by oxygen $2p$ to bismuth $7s$ or $7p$ states.

Additional important information can be obtained from atomic charge bond population. In contrast to plane-wave basis, a linear combination of atomic orbitals (LCAO) basis set provides a natural way of specific quantities such as atomic charge, bond population and charge transfer. Population analysis in CASTEP is performed using a projection of the PW states onto a localized basis using a technique described by Sanchez-Portal et al. [13]. Population analysis of the resulting projected states is then performed using the Mulliken formalism [14]. This technique is widely used for the analysis of electronic structure calculations performed within a framework of LCAO basis sets. Calculated atomic populations, in units of the proton charge for BTBO crystal are presented in Table 3. One can see that the obtained charges calculated using LDA functional are close to the calculated using GGA.

The shortest bond lengths between constituent atoms in BTBO crystal, calculated using LDA and

GGA functional together with overlap populations, are collected in Table 4. As can be seen, the calculated bond lengths and population values are in good agreement between one to another. All bonds of the titled crystal are of covalent type. It is easy to see that B–O bonds possess the highest degree of covalency, while Bi–O—the lowest one. Based on these results, we can conclude that BTBO crystal possesses covalent type of chemical bonding.

Optical properties

The optical properties of solids are described by their dielectric function $\epsilon = \epsilon_1 + i\epsilon_2$, which real part ϵ_1 corresponds to the refractive indices of the material, while its imaginary part ϵ_2 describes the material absorption coefficients, which are directly related to the absorption spectra. The imaginary part of complex dielectric function ϵ_2 , which corresponds to the absorption, can be obtained from the inter-band transition by numerical integration in k -space of elements of dipole matrix operator, between the filled VB states and empty CB levels (Eq. 1):

$$\epsilon_2(\omega) = \frac{2\pi e^2}{\Omega \epsilon_0} \sum_{k,v,c} |\langle \psi_k^c | ur | \psi_k^v \rangle|^2 \delta(E_k^c - E_k^v - E), \quad (1)$$

where E —energy of probing optical beam; u —incident photon polarization vector; ψ_k^c and ψ_k^v —wave functions of the conduction and valence bands in k -space, respectively; Ω —unit cell volume; e —electron charge; ϵ_0 —dielectric permittivity of vacuum; r —operator of electron position; and ω —frequency of incident radiation.

Using Kramers–Kronig relation (Eq. 2) [15] from the imaginary part of dielectric function, its real part can be estimated as follows:

$$\epsilon_1(\omega) = 1 + \frac{2}{\pi} \int_0^\infty \frac{\epsilon_2(\omega') \omega' d\omega'}{\omega'^2 - \omega^2} \quad (2)$$

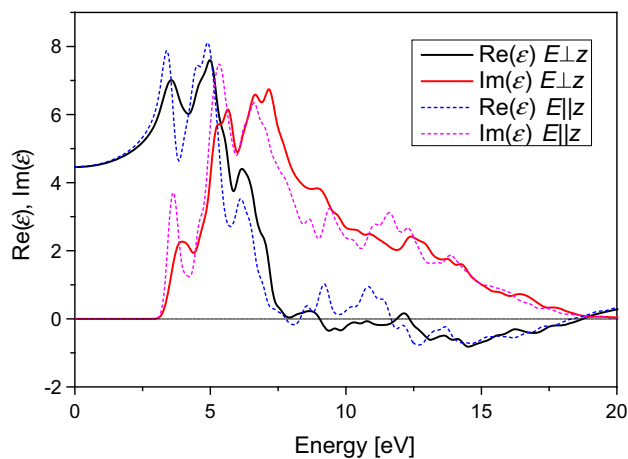
Figure 6 depicts the dispersion of real ϵ_1 and imaginary ϵ_2 parts of dielectric functions calculated using GGA functional. The crystals of hexagonal symmetry have two principal directions that correspond to the direction along polar z -axis and direction perpendicular to z . In Fig. 6, we present the calculated dielectric function, which corresponds to photon polarization $E \parallel z$ and $E \perp z$. The dielectric function shows insignificant anisotropy for BTBO crystal. The real part of dielectric function in the

Table 3 Atomic populations (in units of the proton charge) of the constituent atoms of BTBO crystal (GGA/LDA functionals)

Elements	<i>s</i>	<i>p</i>	<i>d</i>	Total	Charge [e]
B	0.52/0.50	1.65/1.71	0.00/0.00	2.17/2.20	0.83/0.80
O	1.89/1.88	5.12/5.14	0.00/0.00	7.02/7.01	−1.02/−1.01
Te	1.23/1.14	2.06/2.04	0.00/0.00	3.28/3.19	2.72/2.81
Bi	1.91/1.94	1.38/1.40	10.00/10.00	13.28/13.34	1.72/1.66

Table 4 Inter-atomic lengths and overlap populations of the shortest atomic bonds in BTBO crystal (GGA/LDA functionals)

Bond type	Bond population	Length [Å]
B–O	0.79/0.80	1.37743/1.36047
Te–O	0.43/0.44	1.91535/1.89254
Bi–O	0.19/0.16	2.13786/2.16634

**Figure 6** Calculated real $\text{Re}(\epsilon)$ and imaginary $\text{Im}(\epsilon)$ parts of the dielectric functions dispersion for the BTBO crystal using GGA functional.

region from 7.5 to 18 eV has inversion of sign that can correspond to metallic reflection.

Elastic properties

In terms of crystal anisotropy studies, elastic properties of the crystal can be of special interest. The optimized crystal structure of investigated compound as input for the elastic constant simulations was used. The elastic constants are defined by means of the Taylor expansion of the total system energy $E(V, \delta)$, with respect to a small lattice strain δ of the primitive unit cell with volume V . The energy of a strained system is expressed as follows [16]:

$$E(V, \delta) = E(V_0, 0) + V_0 \left(\sum_i \tau_i \xi_i \delta_i + \frac{1}{2} C_{ij} \delta_i \xi_i \delta_j \xi_j \right), \quad (3)$$

where $E(V_0, 0)$ is the energy of the unstrained system with equilibrium volume V_0 , τ_i is an element in the stress tensor and ξ_i is a factor to take care of Voigt index.

For the hexagonal crystal, its elastic properties can be described by asymmetric 6×6 matrix of elastic coefficients. In case of hexagonal symmetry, we get the following relation between elastic constants: $C_{11} = C_{22}$; $C_{13} = C_{23}$; $C_{44} = C_{55}$; $C_{66} = 1/2(C_{11} - C_{12})$; it is known that for practical application it is important to obtain a stable crystal structure. Knowing of the elastic constants and Young's modulus is important for technological aims, in the manufacturing process and crystal preparation. For crystal structure stability of hexagonal symmetry, the obtained elastic constants should satisfy the requirements of mechanical stability criteria [17], which are: $C_{33} > 0$; $C_{44} > 0$; $C_{12} > 0$; $C_{11} > |C_{12}|$; $(C_{11} + 2C_{12})C_{33} > 2C_{13}^2$.

Following Table 5, the calculated elastic constants completely satisfy the mechanical stability criteria. Unfortunately, according to already published data concerning the BTBO crystal, the experimental results of its mechanical properties are not yet known. The values of C_{11} and C_{33} differ one from another, indicating the anisotropy of elastic properties. The universal anisotropy index for BTBO crystal is equal to $A^U = 0.412/0.254$ from the calculation using GGA/

Table 5 Elastic constants C_{ij} and bulk modulus B (in GPa) of the BTBO crystal

Source	B	C_{11}	C_{12}	C_{13}	C_{33}	C_{44}
LDA	76.717	139.58	28.80	58.05	123.28	42.84
GGA	48.238	108.86	15.34	30.27	71.51	29.04

LDA functionals. Calculated elastic compliance matrix S_{ij} for BTBO crystal is presented in Table 6.

The Young’s modulus components E_x , E_y and E_z can be estimated from elastic compliance S_{ij} using following relations: $E_x = S_{11}^{-1}$, $E_y = S_{22}^{-1}$, $E_z = S_{33}^{-1}$. The axial compressibilities k_a , k_b and k_c for hexagonal BTBO crystal are also calculated in the following way [18]: $k_a = S_{11} + S_{12} + S_{13}$, $k_b = S_{12} + S_{22} + S_{23}$, $k_c = S_{13} + S_{23} + S_{33}$. Both Young’s modulus E and compressibility k , calculated using GGA/LDA functionals, are collected in Table 7.

Additional useful method to show mechanical anisotropy can be given by visualization of a three-dimensional dependence of the bulk modulus and Young’s modulus as a function of direction. For hexagonal crystal class, the directional dependencies of bulk modulus and Young’s modulus are given by the following relations [19]:

$$\frac{1}{B} = (S_{11} + S_{12} + S_{13}) - (S_{11} + S_{12} - S_{13} - S_{33})l_3^2, \quad (4)$$

$$\frac{1}{E} = (1 - l_3^2)S_{11} + l_3^4S_{33} + l_3^2(1 - l_3^2)(2S_{13} + S_{44}), \quad (5)$$

where B is the bulk modulus and E is the value of Young’s modulus, in the direction determined by l_1, l_2 and l_3 —the direction cosines of $[uvw]$ directions and S_{ij} are the elastic compliance constants, which are inverse to the matrix of elastic constants C_{ij} calculated for BTBO crystal. The surfaces of directional dependence of bulk modulus B and Young’s modulus E for BTBO crystal, plotted in spherical coordinates, are depicted in Fig. 7.

The surfaces of directional dependence of bulk and Young’s modulus (Fig. 7) show that the BTBO crystal possesses low anisotropy. Both surfaces have the similar shape. In order to receive additional information and a better understanding of bulk modulus and Young’s modulus relation along different directions, the projections of the moduli at ab and ac crystal plane are plotted (see Fig. 8).

Table 6 Calculated elastic compliance matrix (S_{ij}) for hexagonal BTBO crystal (in GPa^{-1})

Source	S_{11}	S_{12}	S_{13}	S_{33}	S_{44}
LDA	0.00891	−0.00012	−0.00414	0.01201	0.02334
GGA	0.01042	−0.00027	−0.00429	0.01762	0.03442

It is easy to see that at ab plane both bulk modulus and Young’s modulus are of a spherical shape, which means in this plane the BTBO crystal is almost isotropic. In the case of ac plane, some anisotropy of mechanical properties is shown.

Effective SHG measurements

Following the performed band-structure calculations and the elastic features, one can expect that the titled crystal may be operated by an external laser light of wavelength near the fundamental absorption edge. For this reason, we used two coherent nitrogen 371 nm 9 ns laser pulses with frequency repetition about 10 Hz in order to study the possible changes of the effective second-order nonlinear optical susceptibilities. As a probing beam, an Er:glass 20 ns laser (at $\lambda = 1540$ nm) was used. The detection was performed using interferometric filter at 770 nm and the photomultiplier connected to the oscilloscope. In order to monitor the possible photoluminescence near 371 nm laser treatment, the additional control of the spectral lines and their time dependencies were performed in the range of 330–905 nm by spectrometer. There was any wider spectral noticeable photoluminescence in this spectral range. Additionally, the time shift between the excitation and the induced nonlinear signals did not exceed few nanoseconds, while for the fluorescence it should be of an order higher. The use of two coherent beams interacting at different angles should stimulate the occurrence of additional birefringence [20], which also changes the nonlinear optical susceptibilities. Moreover, during the photoinduced changes in the common borate crystals, the contributions of anharmonic phonons begin to play an additional role [21, 22]. They may be responsible for the photoinduced second-order nonlinear optical susceptibility changes versus the cationic content, as shown in Fig. 9.

It is crucial that, contrary to the well-studied α -BIBO crystal, for the titled BTBO there exists a huge opportunity to operate the output SHG using external photoinducing UV coherent nanosecond laser pulses. The arrow indicates an excitation of the prevailing number of anharmonic phonons by the nitrogen pulsed laser beams. Because they are anharmonic, their symmetry is the same as for the second-order nonlinear optical susceptibility. As a consequence, it is manifested in Fig. 9 and the optical functions are changed significantly. The effect disappears immediately after the switching off the photoinducing beam treatment.

Table 7 Calculated averaged compressibility (β_H in GPa^{-1}), Young's modulus components (E_x , E_y and E_z in GPa), and axial compressibility (k_a , k_b and k_c in GPa) for hexagonal BTBO crystal

Source	β_H	E_x	E_y	E_z	k_a	k_b	k_c
LDA	0.013	112.223	112.223	83.245	0.00465	0.00465	0.00373
GGA	0.020	95.985	95.985	56.762	0.00586	0.00586	0.00904

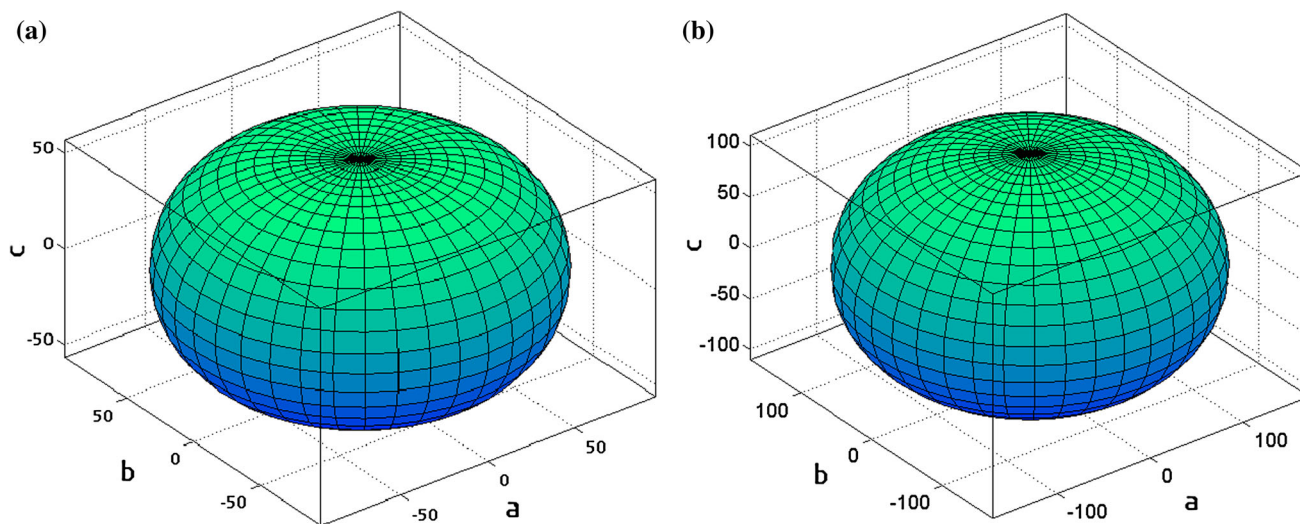


Figure 7 Surface of directional dependence of bulk modulus B (a) and Young's modulus E (b) of BTBO crystal plotted in spherical coordinates.

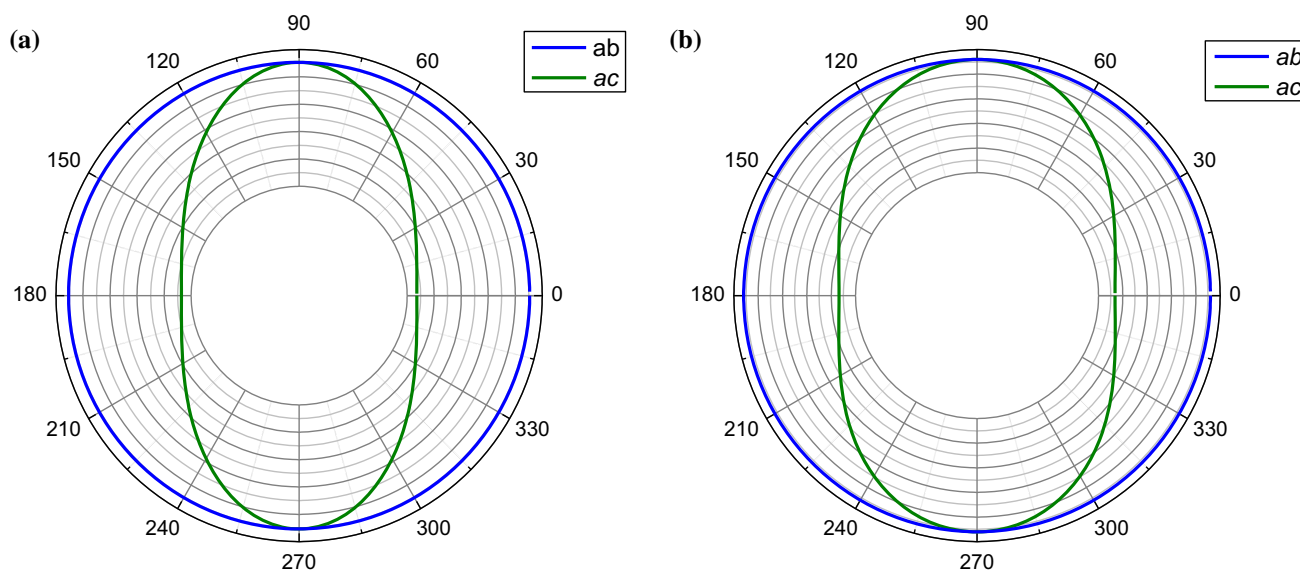


Figure 8 Projection of bulk modulus B (a) and Young's modulus E (b) of BTBO crystal on ab and ac planes.

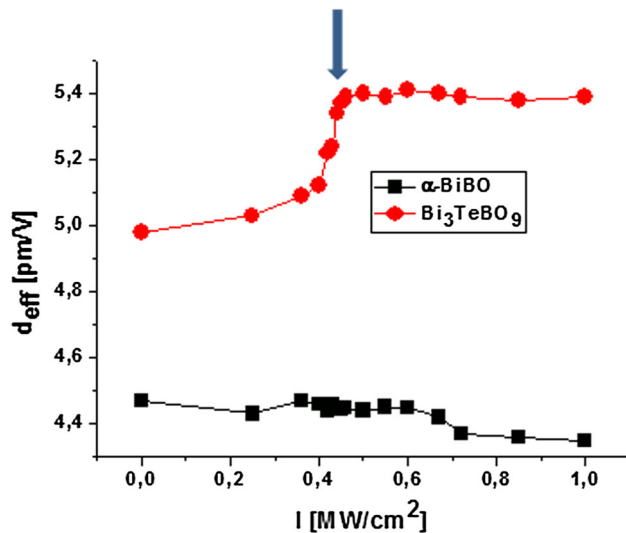


Figure 9 Dependence second-order nonlinear optical susceptibility of BTBO (red plot) at fundamental wavelength 1540 nm versus the power density of the 371-nm pulsed 9 ns laser. The latter is incident under the optimal angle between photoinducing beams equal to about 20 degrees. The arrow corresponds to the critical photoinducing power density at which it gets maximal changes of the second-order susceptibility. The measurement was taken with comparison to α -BIBO (black plot).

Conclusions

An opportunity to influence the second-order nonlinear optical susceptibility of BTBO powder using two coherent beams treatment of 371 nm laser near the absorption edge was established. The performed band-structure calculations and the related elastic properties show that BTBO possesses relatively improved elastic features with respect to other borates. This may favor laser operation with the output second-order nonlinear optical susceptibilities due to changes in microscopical hyperpolarizability. This phenomenon may be a consequence of both the elasto-optical photoinduced anisotropy and possible contribution of the phonon anharmonicities. The comparison with the conventional α -BIBO crystal shows that BTBO is a promising material for the fabrication of UV laser optical triggers.

Acknowledgements

Calculations were carried out using resources provided by Wrocław Centre for Networking and Supercomputing (<http://wcss.pl>), Grant Nos. WCSS#10106944 and WCSS#10106945.

Open Access This article is distributed under the terms of the Creative Commons Attribution 4.0 International License (<http://creativecommons.org/licenses/by/4.0/>), which permits unrestricted use, distribution, and reproduction in any medium, provided you give appropriate credit to the original author(s) and the source, provide a link to the Creative Commons license, and indicate if changes were made.

References

- [1] Kogut Y, Khyzhun OY, Parasyuk OV, Reshak AH, Lakshminarayana G, Kityk IV, Piasecki M (2012) Electronic spectral parameters and IR nonlinear optical features of novel $\text{Ag}_{0.5}\text{Pb}_{1.75}\text{GeS}_4$ crystal. *J Cryst Growth* 354:142–146
- [2] Piasecki M, Lakshminarayana G, Fedorchuk AO, Kushnir OS, Franiv VA, Franiv AV, Myronchuk G, Plucinski KJ (2013) Temperature operated infrared nonlinear optical materials based on Tl_4HgI_6 . *J Mater Sci Mater Electron* 24:1187–1193
- [3] Chung I, Kanatzidis MG (2014) Metal chalcogenides: a rich source of nonlinear optical materials. *Chem Mater* 26:849–869
- [4] Ghotbi M, Sun Z, Majchrowski A, Michalski E, Kityk IV (2006) Efficient third harmonic generation of microjoule picosecond pulses at 355 nm in BiB_3O_6 . *Appl Phys Lett* 89:173124
- [5] Chen C, Sasaki T, Li R, Wu Y, Lin Z, Mori Y, Hu Z, Wang J, Aka G, Yoshimura M, Kaneda Y (2012) Nonlinear optical borate crystals: principals and applications. Wiley-VCH, New York
- [6] Daub M, Krummer M, Hoffmann A, Bayarjargal L, Hillebrecht H (2017) Synthesis, crystal structure, and properties of Bi_3TeBO_9 or $\text{Bi}_3(\text{TeO}_6)(\text{BO}_3)$: a non-centrosymmetric borate–tellurate (VI) of bismuth. *Chem Eur J* 23:1331–1337
- [7] Xia M, Jiang X, Lin Z, Li R (2016) All-three-in-one: a new bismuth–tellurium–borate Bi_3TeBO_9 exhibiting strong second harmonic generation response. *J Am Chem Soc* 138:14190–14193
- [8] Clark SJ, Segall MD, Pickard CJ, Hasnip PJ, Probert MJ, Refson K, Payne MC (2005) First principles methods using CASTEP. *Z Kristallogr* 220:567–570
- [9] Ceperley DM, Alder BJ (1980) Ground state of the electron gas by a stochastic method. *Phys Rev Lett* 45:566–569
- [10] Perdew JP, Zunger A (1981) Self-interaction correction to density-functional approximations for many-electron systems. *Phys Rev B* 23:5048–5079
- [11] Perdew JP, Burke K, Ernzerhof M (1996) Generalized gradient approximation made simple. *Phys Rev Lett* 77:3865–3868

- [12] Pfrommer BG, Cote M, Louie SG, Cohen ML (1997) Relaxation of crystals with the quasi-Newton method. *J Comput Phys* 131:233–240
- [13] Sanchez-Portal D, Artacho E, Soler JM (1995) Projection of plane-wave calculations into atomic orbitals. *Solid State Commun* 95:685–690
- [14] Mulliken RS (1955) Electronic population analysis on LCAO–MO Molecular wave functions. I. *J Chem Phys* 23:1833–1846
- [15] Dressel M, Gompf B, Faltermeier D, Tripathi AK, Pflaum J, Schubert M (2008) Kramers–Kronig-consistent optical functions of anisotropic crystals: generalized spectroscopic ellipsometry on pentacene. *Opt Express* 16:19770–19778
- [16] Ravindran P, Lars F, Korzhavyi PA, Johansson B, Wills J, Eriksson O (1998) Density functional theory for calculation of elastic properties of orthorhombic crystals: application to TiSi₂. *J Appl Phys* 84:4891–4904
- [17] Born M (1940) On the stability of crystal lattices. I. *Math Proc Camb Philos Soc* 36:160–172
- [18] Zahedi E, Xiao B (2015) DFT study of structural, elastic properties and thermodynamic parameters of Bi₂S₃ under hydrostatic pressures. *Comput Mater Sci* 101:301–312
- [19] Dong W, Zhang C, Jiang H, Su Y-H, Dai Z-H (2015) Effect of carbon content and electronic strong correlation on the mechanical and thermodynamic properties of ytterbium carbides. *RSC Adv* 5:103082–103090
- [20] Yanchuk OM, Ebothe J, El-Naggar AM, Albassam A, Tsurkova LV, Marchuk OV, Lakshminarayana G, Tkaczyk S, Kityk IV, Fedrochuk AO (2017) Photo-induced anisotropy in ZnO/PVA nanocomposites prepared by modified electrochemical method in PMA matrix. *Phys E Low-Dimens Syst Nanostruct* 86:184–189
- [21] Majchrowski A, Kityk IV, Mandowska E, Mandowski A, Ebothe J, Lukasiewicz T (2006) Several features of emission spectra of Pr³⁺ ions incorporated into Li₂B₄O₇ glasses. *J Appl Phys* 100:053101
- [22] Kityk IV, Majchrowski A (2004) Second-order non-linear optical effects in BiB₃O₆ glass fibers. *Opt Mater* 26:33–37